Key Points:
- We analyzed the enhanced seismic catalog of a long-lived explosive volcanic eruptive sequence
- Long-period earthquakes track eruptive processes when the system is partially closed and they are not associated with mass ejection
- Volcano-tectonic earthquakes are a secondary effect that does not track the deflation and occur at a low stress-state

Author Contributions:
Conceptualization: Ricardo Garza-Girón, Emily E. Brodsky, Matthew M. Haney
Data curation: Ricardo Garza-Girón, Zack J. Spica, Matthew M. Haney
Formal analysis: Ricardo Garza-Girón, Zack J. Spica, Matthew M. Haney
Funding acquisition: Ricardo Garza-Girón, Emily E. Brodsky

Earthquakes Record Cycles of Opening and Closing in the Enhanced Seismic Catalog of the 2008 Okmok Volcano, Alaska, Eruption

Ricardo Garza-Girón[1] , Emily E. Brodsky[1] , Zack J. Spica[2] , Matthew M. Haney[3] , and Peter W. Webley[4]

[1]Department of Earth and Planetary Sciences, University of California, Santa Cruz, Santa Cruz, CA, USA, [2]Department of Earth and Environmental Sciences, University of Michigan, Ann Arbor, MI, USA, [3]U.S. Geological Survey, Alaska Volcano Observatory, Alaska Science Center, Anchorage, AK, USA, [4]Geophysical Institute, University of Alaska Fairbanks, Fairbanks, AK, USA

Abstract Seismicity during explosive volcanic eruptions remains challenging to observe through the eruptive noise, leaving first-order questions unanswered. How do earthquake rates change as eruptions progress, and what is their relationship to the opening and closing of the eruptive vent? To address these questions for the Okmok Volcano 2008 explosive eruption, Volcano Explosivity Index 4, we utilized modern detection methods to enhance the existing earthquake catalog. Our enhanced catalog detected significantly more earthquakes than traditional methods. We located, relocated, determined magnitudes and classified all events within this catalog. Our analysis reveals distinct behaviors for long-period (LP) and volcano-tectonic (VT) earthquakes, providing insights into the opening and closing cycle. LP earthquakes occur as bursts beneath the eruptive vent and do not coincide in time with the plumes, indicating their relationship to an eruptive process that occurs at a high pressurization state, that is, partially closed conduit. In contrast, VT earthquakes maintain a steadier rate over a broader region, do not track the caldera deflation and have a larger *b*-value during the eruption than before or after. The closing sequence is marked by a burst of LPs followed by small VTs south of the volcano. The opening sequence differs as only VTs extend to depth and migrate within minutes of the eruption onset. Our high-resolution catalog offers valuable insights, demonstrating that volcanic conduits can transition between partially closed (clogged) and open (cracked) states during an eruption. Utilizing modern earthquake processing techniques enables clearer understanding of eruptions and holds promise for studying other volcanic events.

Plain Language Summary Sparse instrumentation and high noise levels prevent us from seeing most of the quakes that occur. This problem is particularly severe during large volcanic eruptions when the explosive processes hide most of the seismic waves. Here, we overcome the problem by utilizing a suite of signal processing methods to dramatically increase our ability to see earthquakes during the noisiest, most difficult to monitor stage of a volcanic eruption. This high-resolution data set unveils features of the volcanic structure as well as the dynamic interaction between the solid medium and the fluids. When the system is closed (clogged), the rocks are stressed by the trapped pressurized fluids and then break in earthquakes. When the system is open (cracked), ash and steam plumes grow higher, the rock is not being stressed as much and the number of observed earthquakes is lower around the eruptive vents. The volcano is displaying both open and closed vent behavior during a single eruption.

1. Introduction

The degree of openness of a volcanic system is recognized as a major determinant of behavior (e.g., Roman et al., 2019; Seropian et al., 2021; Vergniolle & Métrich, 2021). Whether magma or gas can escape determines the state of stress, and ultimately the eruptibility. Similarly, when an eruption begins, the opening of the vent is the most important factor in any subsequent dynamics. Eruptions are often prolonged and complex sequences of events with eruptive plumes separated by quiescent periods, that might be indicative of resealing, changes in magma fragmentation, or exhaustion of supply. Characterizing the eruptive processes is difficult as high temporal resolution of co-eruptive observations requires techniques that can track behavior continuously during one of the most difficult-to-observe periods of the volcanic cycle.

Journal of Geophysical Research: Solid Earth

Investigation: Ricardo Garza-Girón, Emily E. Brodsky, Zack J. Spica, Matthew M. Haney
Methodology: Ricardo Garza-Girón, Emily E. Brodsky, Zack J. Spica
Project Administration: Emily E. Brodsky
Resources: Emily E. Brodsky, Matthew M. Haney
Software: Ricardo Garza-Girón, Zack J. Spica
Supervision: Emily E. Brodsky
Validation: Ricardo Garza-Girón
Visualization: Ricardo Garza-Girón
Writing – original draft: Ricardo Garza-Girón, Emily E. Brodsky
Writing – review & editing: Ricardo Garza-Girón, Emily E. Brodsky, Zack J. Spica, Matthew M. Haney

Volcano seismicity provides a promising road into solving the problem since often the earthquake record provides continuous and highly resolved information. However, seismicity during long-lived, explosive eruptions is practically invisible because of the extreme noise levels of the eruption itself. In a companion paper, we have set out a workflow to solve the detection problem utilizing modern earthquake detection methods (Garza-Girón et al., 2023). As we showed in that paper, we can use a combination of traditional, machine learning and template matching approaches to expand the co-eruptive seismic catalog of the 2008 Okmok Volcano eruption by about a factor of 10. In this paper we now use that catalog to address the first-order questions about co-eruptive seismicity that have not been previously accessible: *What is the relationship between seismicity rate and the eruptive processes? How does the seismicity develop as the volcanic conduit evolves during the eruption?*

Okmok Volcano is a 10-km wide basaltic-andesitic caldera located on Umnak Island, in the Aleutian arc of Alaska (Figure 1). For over a century, most of the eruptions, with a recurrence of about 10 years (the last of which occurred in 1997), had their source at an intra-caldera cone (Cone A; Figure 1 inset) and were mostly Hawaiian to Strombolian (Coats, 1950; Grey, 2003). The 12 July 2008 eruption, which was given a scale of 4 in the Volcanic Explosivity Index (VEI), marked a change in this behavior because of the interactions between magma and water, making new intra-caldera maars and developing a new tephra cone during a large phreato-magmatic eruption (Larsen et al., 2015). Since the island has a topographical regional-scale tilt toward the northeast, the northern sector of the caldera is characterized by larger bodies of surface and groundwater, with approximately 10^{10} kg of water available for the 2008 eruption (Unema et al., 2016). Multiple geophysical studies, most of which focused on modeling the source of geodetic deformation, have found the location of a shallow (2–4 km) magma reservoir at approximately the same location beneath the caldera (Albright et al., 2019; Biggs et al., 2010; Fournier et al., 2009; Freymueller & Kaufman, 2010; Lu & Dzurisin, 2010; Mann et al., 2002; Masterlark et al., 2010; Wang et al., 2021; Xue et al., 2020). Furthermore, different authors have shown that inflation cycles started immediately after the end of the deflationary eruptive periods in 1997 and 2008, suggesting a quick replenishment of the shallow magma reservoir to compensate the pressure gradient (Freymueller & Kaufman, 2010; Lu et al., 2005; Lu & Dzurisin, 2010; Wang et al., 2021).

During the 6 months preceding the eruption, the Alaska Volcano Observatory (AVO) detected only nine low magnitude ($M \leq 2.6$) earthquakes, although many of the stations in the region had outages during those months. Most of the inter-eruptive seismicity is localized in a geothermal field on the isthmus of Umnak Island inland from Inanudak Bay (Figure 1). The only precursory activity to the eruption came on 12 July 2008, when the seismic network at Okmok Volcano recorded the onset of a ~4.5 hr-long earthquake swarm (Johnson et al., 2010; Larsen et al., 2009) after which explosive activity commenced. The short sequence of precursory earthquakes was reanalyzed by Ohlendorf et al. (2014) using the AVO catalog, and the earthquakes originated at approximately 3 km depth beneath the intra-caldera cone known as Cone D (Figure 1 inset). The beginning of the eruption was marked by a large-scale sub-Plinian explosion that released a ~16 km above sea level (ASL) high dark plume, consistent with a VEI 4 eruption (Newhall & Self, 1982). This plume was accompanied by more than 12 hr of continuous high-amplitude seismic eruption tremor (Larsen et al., 2009). Tremor continued at variable levels throughout the 40-day-long eruption and emanated mainly from a new intra-caldera cone (Haney, 2010, 2014). This new cone, to the north of Cone D and built during the 2008 eruption, was subsequently named Ahmanilix, which means "surprise" in the language of the Unangan people whose ancestral lands include Umnak Island (Larsen et al., 2015). After the initial plume, the activity continued by the opening, and perhaps widening, of new vents in a westward alignment from the north-west of Cone D. On July 19, the network recorded high-amplitude continuous tremor that lasted ~20 hr and is thought to be related to the initiation of the temporary drainage of the perennial North Cone D Lake (hereby called North Lake) (Figure 1). The drainage of the lake was verified by satellite imagery on July 24, and standing water was observed again at the lake on August 1 (Larsen et al., 2015). Moreover, Larsen et al. (2015) reported that between July 24 and August 1 the North Vent structure, directly to the north of Ahmanilix, widened and there was an increase in number and size of reflectors observed in Synthetic Aperture Radar (SAR) images, accompanied by an increase in ash production from August 1 until August 3, confirmed by AVO staff in the field. From August 3 until August 19, when the last emission of ash was reported and the eruption officially ended, the plumes decreased in number and size.

Here, we provide a detailed seismological perspective of the eruption by analyzing the enhanced earthquake catalog. After briefly describing the methods of measuring seismicity rate, clustering and magnitude distribution, we present the resultant rates of both LP and VT earthquakes. The two types of earthquakes show distinct trends with the LPs clustering around the eruptive plumes, likely indicating a period of clogging and overpressure, and
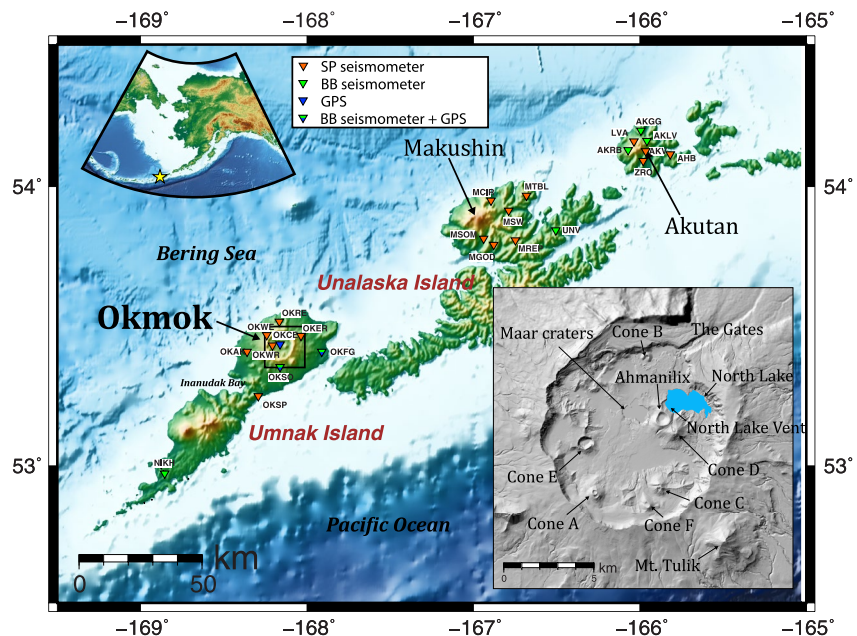
Figure 1. Map of the study region. Stations (orange: short-period seismometer; green: broadband seismometer; blue: GPS) used for this study with an inset showing the location of the intra-caldera cones and the most important features of Okmok Volcano. Inset corresponds to black rectangle in the larger map.

the VTs continuing steadily during the eruption, likely as result of the pervasive stresses in the solid edifice. The distinction continues through the final closing sequence of the eruption. The only notable exception is the initial opening sequence, as we will discuss below. Ultimately, we conclude that LP earthquake rates are highest in clogged periods when there is no eruptive plume and lowest when the vent is cracked open and discharging, while VT earthquakes reflect the stressing regime primarily through their *b*-values rather than their locations and timing.

2. Data and Methods

We discuss the creation of the enhanced seismic catalog in our complementary paper (Garza-Girón et al., 2023). This high-resolution catalog was built using continuous seismic waveform records from seven broad-band and 16 short-period instruments of the AVO and the Alaska Earthquake Center (AEC) networks (Figure 1) and multiple earthquake detection algorithms in tandem. Two machine learning algorithms and the original analyst catalogs were combined to form a library of templates that were then used to expand the catalog further. Locations for the catalog were determined and then the relative relocations were found using two different algorithms: hypoDD and Grow-Clust (Trugman & Shearer, 2017; Waldhauser & Ellsworth, 2000). Once locations were determined, local magnitudes were estimated using a local amplitude attenuation relationship. Magnitudes were consistently calculated for all types of events. Finally, the catalog was divided into two classes of events based on their spectral content: high-frequency volcano-tectonic (VT) events and long-period (LP) events (Figure 2). VTs show most of their power above 5 Hz, while the LPs have most of their energy below the 5 Hz threshold. The distribution of percentage of energy below the 5 Hz threshold is bimodal, suggesting that the catalog is predominantly composed of two classes of events. Further details, including a discussion of uncertainties, are available in Garza-Girón et al., 2023.

The original AVO catalog reported 434 events from 1 June 2008 to 30 August 2008. In the new catalog (Figure 2), there are a total number of 3,101 earthquakes (2,169 VTs and 932 LPs), 3,041 of which have a magnitude estimation (2,154 VTs and 887 LPs), 2,089 were successfully relocated by hypoDD, and 1,398 were relocated by GrowClust. For the analysis of this paper, we selected events that were located using a minimum of five stations (1,334 for hypoDD and 983 for GrowClust). We used the catalog relocated with hypoDD, which permitted more relocations than GrowClust, and we compared the two different relocation catalogs when appropriate to guarantee the robustness of the observations. All the interpretations derive from observations that are present in both relocated catalogs as illustrated in Supporting Information S1 (Figures S1–S4).
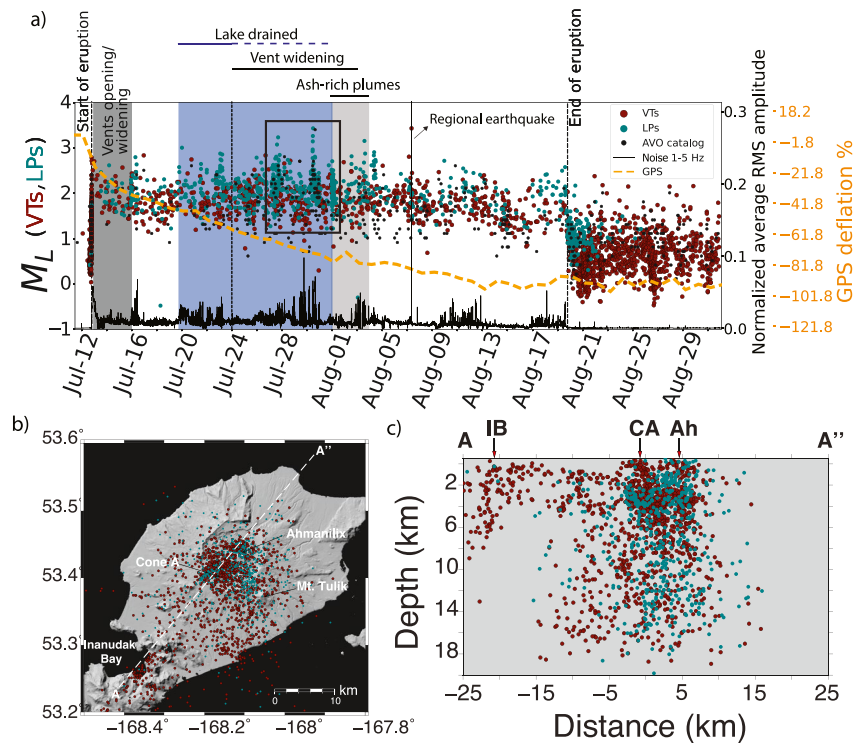
Figure 2. Overview of earthquake catalog and chronology. (a) Magnitude of all earthquakes separated by their classification (VTs = red, LPs = turquoise) and contextual deflation, seismic amplitude and narrative data. The deflation percentage is derived from GPS by Freymueller and Kaufman (2010) (orange dashed curve, right-hand axis in matching color). Shaded background and annotation indicate major periods in the eruption chronology of Larsen et al. (2015). Black rectangle indicates the interval of bursts of migrating LPs discussed in text. The black line is the average RMS amplitudes in the two broadband stations (OKFG and OKSO) at 1–5 Hz measured every 5 min. The large spike in RSAM on August 7 corresponds to a regional earthquake that was picked up by the network. (b) Map and (c) cross-sectional view of the relocated VTs (red) and LPs (turquoise). A vertical exaggeration factor of 1.4× was applied to (c). Width of cross-section = 4 km; azimuth = 40°. Arrows: IB = Inanudak Bay; A = Cone A; Ah = Ahmanilix.

2.1. Earthquake Rates

A key question in understanding and monitoring volcanic eruptions is the relationship between the changes in the observed seismicity rate and the evolution of the eruption. The detection methods deployed allow us to ask this question even during the high noise levels of the eruption. However, noise levels may fluctuate; thus, comparing the observable seismicity rate over time requires a correction for variable detection levels due to noise.

Therefore, we calculated the seismicity rate separately for the three different stages of eruption: pre-eruptive, co-eruptive and post-eruptive. For each period, we computed the completeness magnitude using the maximum curvature method plus a correction of 0.1 to compensate for the common underestimation of M_c (Table S1 in Supporting Information S1; Wiemer & Wyss, 2000). Magnitudes were rounded to two significant figures (i.e., $\Delta M = 0.01$). We counted the events above M_c using moving time windows of different sizes to estimate the observable seismicity rate. In choosing different time windows, we are effectively applying a low-pass filter to the seismicity rate sequence and different periods will give information at different temporal resolutions. Therefore, we present a long-period trend (earthquakes every 48 hr) to show a global perspective of the rates during the whole eruptive process and we also provide a highly sampled rate (earthquakes every 4 hr) to analyze the behavior of VT and LP earthquakes in detail during the most critical stages of the eruption.

2.2. Earthquake Clustering

The cross-correlation of volcanic earthquakes to detect earthquake clusters or multiplets is common practice in studying volcanic processes (e.g., Buurman et al., 2006; Petersen, 2007; Thelen et al., 2011; Umakoshi et al., 2008). In this paper, we use this technique not to find multiplets or families of earthquakes but rather

to create more insight into the dynamics of the eruptive process at Okmok Volcano. Our method is as follows: 3 s of the waveforms of each event in all available stations (0.2 s before P—2.8 s after P) is analyzed with all waveforms processed by removing the mean, applying a linear detrending and a 5% Hanning window taper and filtered between 3 and 10 Hz. Using these waveforms, we created a cross-correlation matrix based on the average cross-correlation across all synchronous stations for each pair of events. The matrix distinguishes the events that are well-correlated and thus quantitatively support the existence of bursts.

2.3. Magnitude Distributions

Variations in magnitude distributions are captured by variations in the b-value of the Gutenberg-Richter distributions where the number of earthquakes of magnitude greater than or equal to M is proportional to 10^{-bM}. The b-value is commonly estimated with a maximum likelihood estimator that requires knowledge of the minimum magnitude at which the detection level is near 100% (Aki, 1965; Utsu, 1965). This sensitivity to the completeness level is problematic for the Okmok Volcano data, where noise level is constantly changing. Consequently, we utilized the b-positive (b^+) method recently introduced by Van der Elst (2021) that uses the inter-event magnitude differences, which follow a distribution of the same functional form as Gutenberg-Ricther. As can be seen from the positive differences' distributions (Figure S5 in Supporting Information S1), the major advantage of the b^+ estimate is that it provides robust measurements of b-values without explicitly requiring an estimate of the completeness magnitude. It is not as strongly biased by its value as the maximum likelihood procedure. We calculated the uncertainty of each b^+ measurement by bootstrapping the magnitude difference distribution 300 times and estimating the standard deviation of the bootstrap realizations.

The b-value variations require a significance test. Since the distribution of the differences in magnitudes has the same mathematical form as the distribution of the magnitudes (Van der Elst, 2021), we calculated the probability that two different b^+ values come from the same populations using the Utsu test (Gerstenberger et al., 2001; Schorlemmer et al., 2005; and references thereafter) to establish the statistical significance of our results. This test was derived for the commonly used b-value, and the resulting probability P of randomly obtaining the observed result is:

$$P \approx e^{\left(\frac{-dA}{2}-2\right)},$$

(1)

and the parameter dA is defined by:

$$dA = -2N \, ln(N) + 2N_1 \, ln\left(N_1 + \frac{N_2 b_1}{b_2}\right) + 2N_2 \, ln\left(N_2 + \frac{N_1 b_2}{b_1}\right) - 2,$$

(2)

where N_1, b_1 and N_2, b_2 are the number of events and b values in groups 1 and 2, respectively, and the total number of events is N, which is equal to $N_1 + N_2$.

3. Results: The Sequence of the Eruption as Shown by the Enhanced Catalog

Figure 2 presents an overview of the co-eruptive VT and LP magnitudes in context of the major eruptive events as recorded by the deformation, seismic noise and narrative data. There is a notable lack of low magnitude VT and LP events recorded during the eruption that correlates with an increase in the 1–5 Hz Real-time Seismic Amplitude (RSAM) (i.e., tremor noise level; Figure 2a). Interestingly, the change in magnitude of completeness before, during and after the eruption matches almost exactly the sequence of earthquakes observed for the 2021 eruption in La Palma, Canary Islands (see Figure 7a of D'Auria et al., 2022). The RSAM shown here is the root-mean-square (RMS) seismic amplitude in 5-min windows, averaged across the two broadband stations (OKFG, OKSO). The drop in RSAM at the end of the eruption seen in Figure 2 corresponds to the improved detection of small earthquakes (Figure 2) as well as the reduced magnitude of completeness after the eruption (Figures S6 and S7 in Supporting Information S1).

The high co-eruptive tremor noise level justifies the specialized methods required in this study. These methods have detected nearly an order of magnitude more events than originally recorded (black data points in Figure 2a), but do not completely solve the problem that the detection of small events is challenging during an eruption. Nonetheless, as will be discussed below, the improved catalog not only illustrates seismicity rate changes and
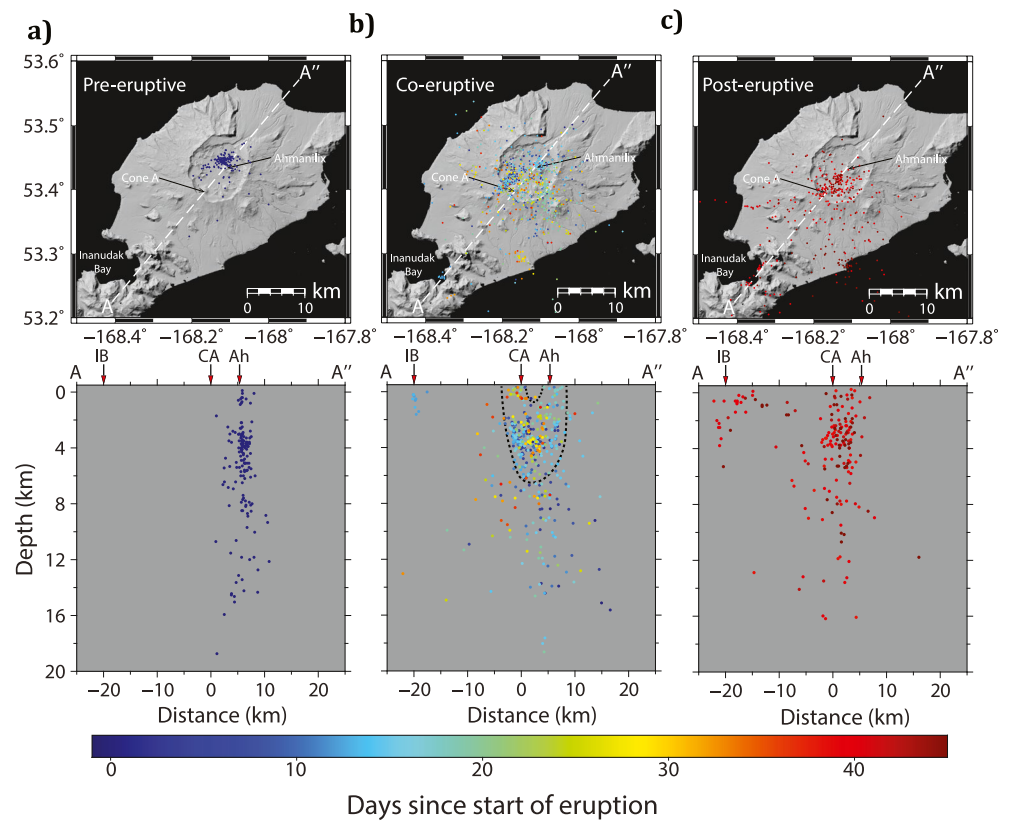
Figure 3. HypoDD relocated events before (a), during (b) and after (c) the eruption. The sequence leading up to the eruption clusters underneath the vents that developed during the eruption. The co-eruptive seismicity shows a bowl-shaped volume inside the caldera with most of the activity occurring under Cone A and Ahmanilix. The post-eruptive sequence has earthquakes in the south sector of the caldera primarily in the vicinity of Cone (a) A vertical exaggeration factor of 2.5× was applied to the cross-sections. Cross sectional width = 3 km/azimuth = 40°. Arrows: Ah = Ahmanilix; CA = Cone A; IB = Inanudak Bay.

changes in magnitude distributions that help understand the open and closed dynamics of the 2008 eruption, but it also illuminates the structure of the volcano with improved resolution. To put it into perspective, the number of earthquakes detected and located during the 1.5 months period of the eruption (3,101) is comparable to the total number of earthquakes reported in the catalog from 2001 to 2018 (3,002; Power et al., 2019), and the earthquakes relocated with hypoDD (2,898) represent ~99.56% of the earthquakes in the catalog.

A first inspection reveals patterns in the enhanced catalog that mimic the observational chronology of the eruption from Larsen et al. (2015) (shaded areas) and the GPS data from Freymueller and Kaufman (2010) (Figure 2). For example, the first burst of LP events occurs right after the initial phase of vents opening/widening (July 16), after which there is a change in the slope of the GPS decay at OKFG. Also, the most notable increase in LP activity is during the middle of the eruption (black box in Figure 2a) and it matches well with the periods when Larsen et al. (2015) observed further widening of the North vent (see Figure 1 for location), and the largest bursts occur before, during and after a period of increased ash content observed in the eruptive plumes. The GPS curves represent the time series of the radial displacements detrended and normalized using the quiescence period between 2005 and 2008, so 0% GPS inflation represents the value at the beginning of 2008 (Freymueller & Kaufman, 2010). In this sense, the GPS deflation % shows how representative is the pre-eruptive inflation and co-eruptive deflation relative to the background. Assuming a stationary deflation source, the GPS indicates that the caldera subsurface was slightly inflated at the onset of the eruption and it generally deflated rapidly during the eruption before slowing down during the final sequence.

Most of the seismicity leading up to the eruption is tightly clustered underneath the area where the main eruptive vents formed and almost all the earthquakes were classified as VTs (Figures 2 and 3a). The co-eruptive seismicity is essentially localized in and around the volcano's caldera in a bowl-shaped volume (Figure 3b, Figures S3b and S4b in

Supporting Information S1). This population includes LP events that are well-clustered near the active vents, as well as near Cone A, and VTs that are more broadly distributed but are also sporadically clustered near Cone A. Finally, most of the seismicity after the last plume emission is in the southern sector of the caldera near Cone A (Figure 3c).

Reassured by the general correspondence of the chronology, we now move onto a systematic comparison of the relationship of the LPs and VTs to the eruptive events and the relationship of the seismicity to the structure of the volcano. We separate our findings into five key observations.

3.1. Observation 1: Co-Eruptive LP Earthquakes Related to Venting Processes and VT Events Independent of Plumes

3.1.1. Seismicity Rate Indicates the Difference Between LPs and VTs

To understand how seismicity relates to the eruptive processes, we measured a long period (48-hr) and high-temporal resolution (4-hr) seismicity rate for the VT and LP populations and compared the time series to the reported plume heights (Larsen et al., 2009) and GPS time series data (Figure 4).

To ensure the accuracy of the timing of the plume height data during the middle of the eruption, we cross-checked the times against Advanced Very High-Resolution Radiometer (AVHRR) satellite observations (Figure S8 in Supporting Information S1). If there were plumes reported during times when the satellite imagery does not show any evidence of emissions (see Figure S8 in Supporting Information S1) we removed the reported plumes from the data set. There is one time period, however, when emissions are clearly observed in the satellite images, but no plumes were reported (July 31 12:30 to July 31 21:30); we mark this time period with a dashed gray box in Figures 4 and 5.

The long-period (48-hr) seismicity rate (Figures 4a and 4b) reveals an interesting first order observation for the co-eruptive stage: the LPs track the eruptive activity, whereas the VTs are independent of the plume observations.

The first burst of LPs is observed after the initial phase of opening and widening of the main vents (July 13–16). After this, the LP rate shows a swarm-like pattern (Benoit & McNutt, 1996; Mogi, 1963; Zobin, 2012) with a large increase in rate of almost two orders of magnitude starting around July 20, following a cluster of plume observations. The swarm-like pattern peaks around the middle of the eruption (July 27) and then quickly decreases toward August 8. The end of the eruption (~August 8–18) is marked by a substantial reduction of the LP rate, but immediately after the last plume emission (August 19), when the eruption officially ended and the volcano remained as a closed system, there was a large burst of post-eruptive LPs that decayed rapidly.

The peak of the swarm pattern (July 27) is the most significant co-eruptive seismic sequence. This period matches the widening of North Lake vent observed in SAR images (Larsen et al., 2015) and an increase of ash-rich plumes. As mentioned above, the long-period (48-hr) rate shows that the LPs are related to eruptive activity. However, and importantly, the short-period (4-hr) rates show that the LP bursts are not coincident in time with observations of large plumes from satellite images or written reports from AVO (Figure 4d). The discrepancy between increased LP rates and plume observations does not correspond to changes in noise or to missing data (Figure S9 in Supporting Information S1).

The behavior of the LP events can be contrasted with the VT events. VT earthquakes maintain a steadier seismicity rate during the eruption compared to the LPs. The VTs are also more distributed over a large region (Figures 2b and 2c) and do not decrease (or increase) in the period that the GPS shows a changing deflation rate (Figures 4a and 4c). Apart from the initial opening sequence, which we will address separately below, the VTs show a relatively stable rate until the onset of the widening of the North vent reported by Larsen et al. (2015) (July 24 to August 3), when the rate increases by a factor of two. The VT rate has slight variations during the rest of the eruption (Figures 4a and 4c) but overall gradually decreases until the cessation of activity. The post-eruptive rate for the VTs shows a large jump of about an order of magnitude compared to the co-eruptive rate, and decays gradually, once again differentiating from the LPs rate behavior. Overall, the VTs rate is steadier than the LPs rate throughout the co-eruptive and post-eruptive phases of the eruption, and it does not correlate or anti-correlate with other geophysical observations.

3.1.2. Cycles of LPs and Plumes

The difference in the overall behavior of the seismicity rate between VTs and LPs (i.e., relatively stable vs. significantly variant), along with the LPs relation with plume activity, hints at different controlling mechanisms for the two types of signals throughout the eruption. To further investigate this, we inspected the middle stage of the eruption in more detail, when the rate of the LP seismicity is at a cusp and Larsen et al. (2015) report the widening of the vents and a richer content of ash in the plumes. It is worth noting again that most of the VTs
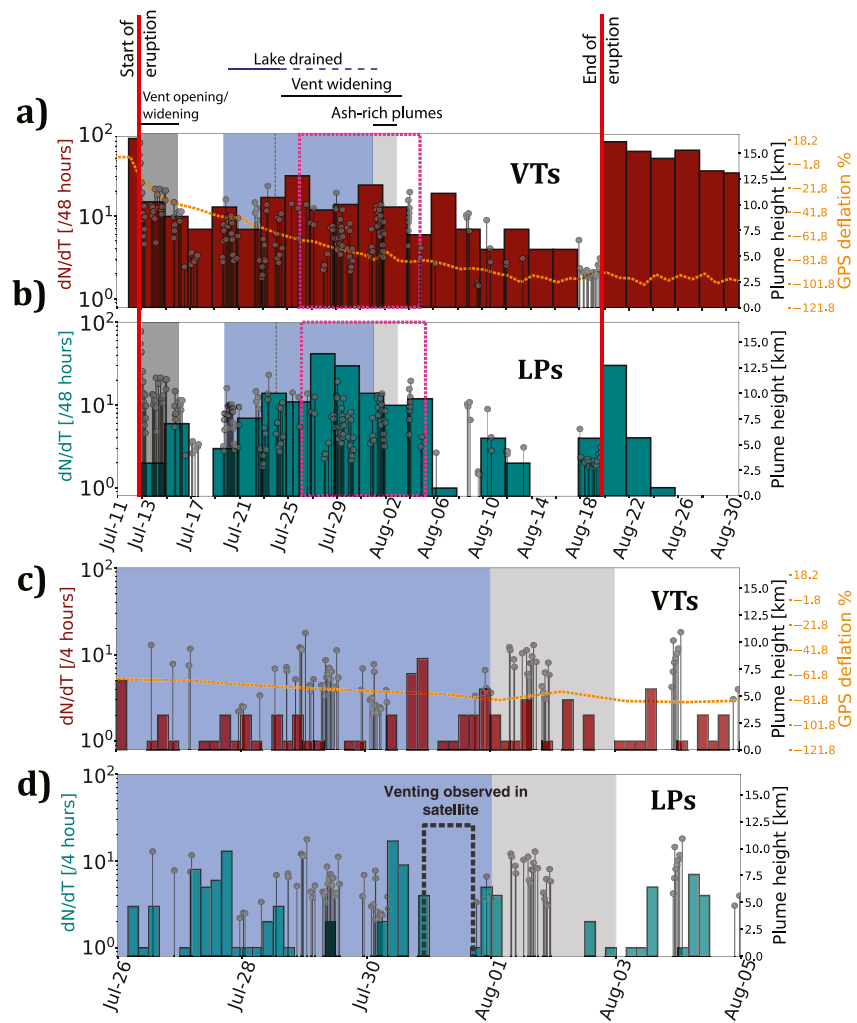
Figure 4. Seismicity rate over time. Number of earthquakes every 48 hr for the eruptive sequence separated into pre-, co- and post-eruptive phases for VTs (a) and LPs (b), and a higher resolution (earthquakes/4 hr) rate for VTs (c) and LPs (d) for the middle of the eruption (magenta frame in a,b). Note that the seismicity rate for the three eruptive phases in (a) and (b) has a different completeness level (see Figure 2, Figures S6 and S7 in Supporting Information S1) and thus trends should only be interpreted within each time interval. VT earthquake rates and LP earthquake rates are shown in red and turquoise, respectively. GPS deflation percentage is shown with the dashed orange dashed line and the plume height observations (Larsen et al., 2009) are shown in gray. Dashed gray box shows a time period with otherwise unreported satellite observations of plumes (see text). Shaded areas correspond to the eruption chronology as shown by the horizontal lines above panel (a).

are more distributed in the caldera, with certain bursts around Cone A, while the majority of the LP earthquakes are highly clustered in the vicinity of the active vents and near the east side of the caldera rim (Figures 2b and 2c).

The middle sequence of the eruption probably initiated with the drainage of North Lake on July 19 and an ensuing escalation in continuous tremor (Larsen et al., 2015). This stage is marked by the largest number and magnitude of LP events. Throughout this period, bursts of LPs migrated from directly underneath Ahmanilix at 2–5 km depths (July 27), then progressed either to the southeast toward Cone D or to the east toward North Lake and clustered at shallower (~1 km) depths (July 30), and finally migrated east and south toward the caldera wall and Mount Tulik from July 31-August 1. Figure 5a shows the time series of the magnitudes of the LP events color coded by time since July 27, and Figures 5b–5e show the relocations of the earthquakes' hypocenters, where the migration from Ahmanilix to the caldera wall can be observed. Like Figure 4, the bursts of migrating LPs do not coincide in time with plume observations. This is even more evident when compared to the envelope of the time series (orange curve on Figure 5a), where the peaks correspond to the bursty character of the LPs sequence, and the troughs are matched by an increase in plume observations. There were at least three cycles of LP bursts during
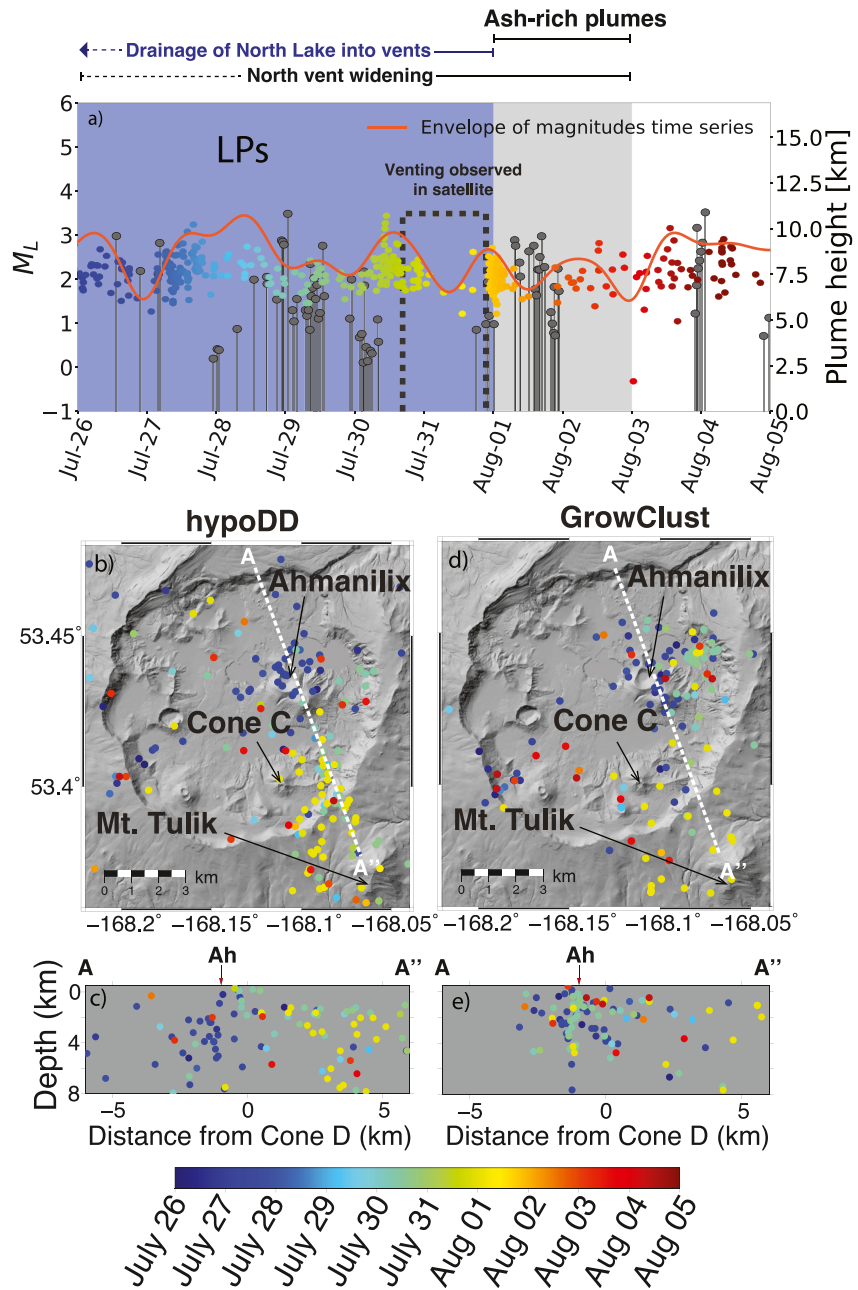
Figure 5. Migration of LP bursts during the middle of the eruption and lack of correspondence with plumes. (a) Magnitudes over time for the LP bursts during the middle of the eruption. The orange curve shows the magnitude envelope. Plume height observations are shown in gray stems. (b) Map and (c) cross-sectional view of the LP earthquakes (hypoDD relocations) during the most prominent bursts from July 27 to August 1, showing the migration pattern. All LPs are colored by days since July 27. (d) and (e) are GrowClust relocations. Note the criteria of the GrowClust algorithm results in fewer located events. A vertical compression factor of 2.1× was applied to (c) and (e). Width of cross-section = 3 km; azimuth = 160°. Arrows: Ah = Ahmanilix.

the middle of the eruption. The striking correspondence of the magnitudes envelope troughs to plumes even warned of a lack of plume observations during July 31. After a manual inspection of the available AVHRR images (Figure S8 in Supporting Information S1) we could confirm that, indeed, emissions were present at those times.

Interestingly, a second escalation in steady tremor on August 2, after the bursts of migrating LP events, migrated from North Lake to the caldera wall over a period of 1–2 hr (Haney, 2014) and was accompanied by a transient inflation signal in the GPS.

3.2. Observation 2: Opening Sequence

A major exception to the LP and VT behavior discussed above is the initial opening sequence of the eruption. The overall rate of the VT events (Figure 4a) is characterized by a single sharp burst (interpreted as run-up seismicity leading to the eruption), followed by a rate decrease of about one order of magnitude.

The opening sequence is entirely composed of VT earthquakes, and it extends to at least 14 km depth. The magnitudes during this runup period show a gradual increase leading to the onset of the eruption (Figure 6a). The seismicity is broadly distributed about the apparent injection dyke (Figures 6b and 6c) and its end is marked by a migration over several minutes from Ahmanilix (i.e., the eruptive vent) toward the center of deformation the west (Figures 1 and 6d,e). This observation contrasts what has been observed in some other large basaltic volcanoes, where the migration of earthquakes before the onset of the eruption is toward the eruptive site (Caudron et al., 2015; Duputel et al., 2019; Lengliné et al., 2021).

The earthquakes of the opening sequence are well-located underneath the ultimate eruptive vents at ~4–7 km depths. There is only a small cluster of shallow earthquakes underneath the maars craters that could be an indication of more vigorous hydro-magmatic interactions prior to the initial explosions. Earthquakes are absent at shallower depths under the vents during this period.

Ohlendorf et al. (2014) describe the earthquakes hypocenters of the opening sequence as a shallow (<6 km) planar feature striking WSW-NNE and dipping to the NNW. Our enhanced catalog illuminates an elongated structure striking W-E and dipping to the SE down to a depth of ~15 km (Figure 3a and Figures 6b–6d). The earthquakes that are observed up to 3 hours before the eruption span the whole dipping structure and they have a small magnitude; however, during the last hour preceding the start of the eruption the earthquakes started concentrating at shallower depths (3–6 km). These results confirm the observations by Ohlendorf et al. (2014) on the progression of the earthquakes during the last minutes before the eruption, although the direction of the dip of the planar feature that Ohlendorf et al. report differs from our results.

3.3. Observation 3: The Closing Sequence of LP and VT Earthquakes

The cessation of eruptive activity is marked by a sudden burst of LP earthquakes, which decayed rapidly with time, and was accompanied and followed by a steady stream of small VT earthquakes that occur south (and therefore distinct) from the previous concentration of seismicity. Shortly after the last plume of the eruption, the average RSAM reduced and there was a major increase in the number of small earthquakes observed in the southern sector of the caldera and in distributed seismicity all over the southern part of the greater Okmok Volcano, all the way south to the isthmus of Umnak Island (Inanudak Bay, Figure 1). The post-eruptive seismicity involves a burst of LPs that started immediately after the last plume emission, and decayed rapidly with time, besides a high production of VT earthquakes that decayed slowly with time (Figures 4a and 4b). This post-eruptive population represents almost 40% of all the earthquakes detected from June 1 to August 31.

Surprisingly, there are very few earthquakes close to Ahmanilix or the other vents; rather, they are almost completely localized at the center of the caldera and under Cone A at ~4 km depth (Figure 3c), which is the depth of the estimated magma reservoir.

The end of the eruption also showed a change in geodetic behavior. Freymueller and Kaufman (2010) discuss the changes in the GPS deflationary trend that started 2–3 weeks after the main ash emissions based on a change in rate in the two GPS stations outside the caldera (OKSO and OKFG). Deflation was still ongoing until at least late September on OKFG, but an inflationary signal inside the caldera was recorded by station OKCE within 3 weeks of the end of the eruption (there is an ambiguity on the exact timing due to a data gap). Freymueller and Kaufman (2010) interpreted this as the result of deflation in a deep source and the immediate inflation of a shallow source.

3.4. Observation 4: VT *b*-Value Changes

The notion that *b*-values have a stress dependence and that tracking *b*-values over space and time can illuminate changes in the stress field is a common tenet in seismology (Scholz, 1968, 2015); variations in *b*-values have also been broadly explored in volcanoes (e.g., Bridges & Gao, 2006; Garza-Girón, 2014; Wyss et al., 2001) and low *b*-values are commonly interpreted as indicating high deviatoric stress. Since these theoretical principles apply to the accumulation of stress on rocks and their eventual failure, we focus our *b*-value analysis on VT events, which represent the brittle failure of rocks (Roman, 2005). According to the above thinking, the *b*-values of the
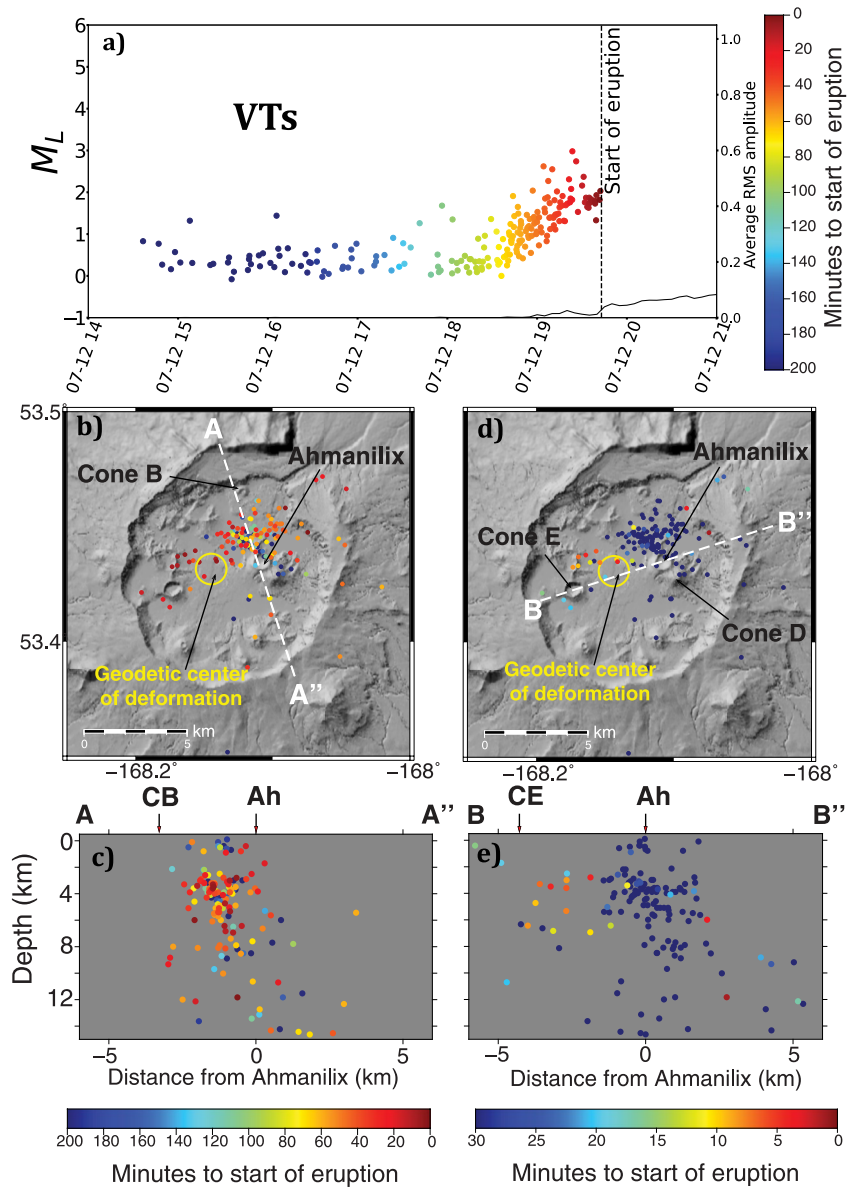
Figure 6. Timing (a) and location (b)–(e) of the VT sequence before the start of the eruption on July 12 19:43 UTC. Panels (a)–(c) have a color scale saturated at 200 min and panels (d)–(e) color scale saturates at 30 min before the eruption to show the migration of earthquakes toward the 2008 deflation source (yellow circle; Lu & Dzurisin, 2010) minutes before the start of the eruption. The azimuth of the cross-sections in (c) and (e) are 342° and 252°, respectively. A vertical compression factor of 2.1× was applied to (c) and (e). Width of cross-sections = 5 km. Arrows: Ah = Ahmanilix; CE = Cone E; CB = Cone (b).

VT earthquakes should indicate the response of the host rocks of the volcano to the stress induced by the injection and extraction that undoubtedly took place before, during and after the eruption.

Figure 7 shows time variations of the b^+ estimator of the b-value, which is calculated as discussed in Section 2.3, for the opening, co-eruptive and closing stages; the uncertainties shown in Figure 7 represent the standard deviation of 300 bootstrap realizations. All the 1-P values (P being the probability that two b-values come from the same population; Equation 1) for all the combinations of pairs of b^+ and b-values for the co-eruptive phase compared to before or after the eruption are lower than the 99% confidence limit, so we conclude that our results are highly statistically significant (Tables TS1 and TS2 in Supporting Information S1). The co-eruptive VTs have a larger b^+ than before or after the eruption. Even though the magnitudes of the earthquakes observed during the eruption are the highest, their distribution seems to favor smaller earthquakes, giving a relatively high b^+ (1.39 ± 0.07). Earthquakes in the opening and post-eruptive stages have a lower b^+ (1.13 ± 0.1 and 1.11 ± 0.05, respectively),
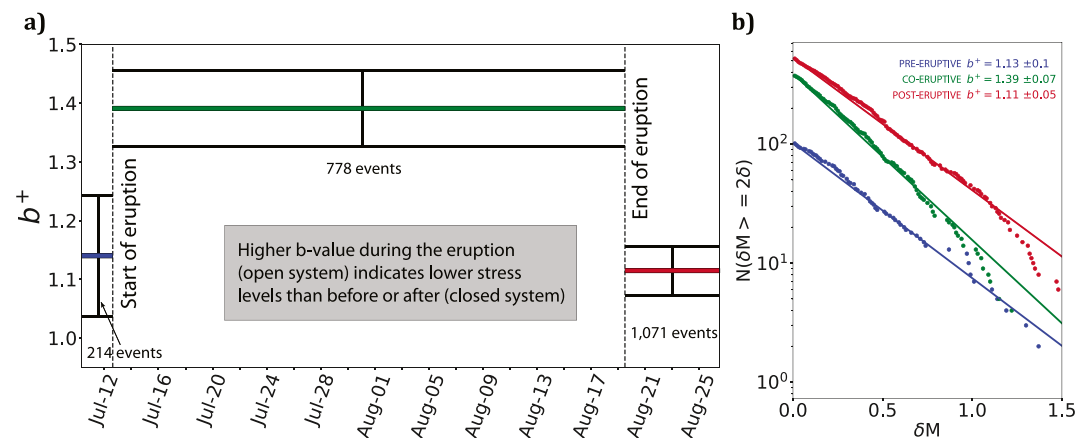
Figure 7. b^+ before, during and after the eruption for VT earthquakes. (a) The pre- and post-eruptive periods show a lower b^+, suggesting higher stress levels. The error bars are the standard deviation of 300 bootstrap realizations. (b) Cumulative distribution of positive magnitude differences between consecutive earthquakes and the best-fit b^+ for each stage of the eruption.

thus, the b-value would indicate that the stress level was higher during the pre- and post-eruptive periods. We also calculated the temporal variations of the b-value using a maximum-likelihood estimation (Aki, 1965; Utsu, 1965) and a least-squares computation. Even though they perform poorly compared to b^+, we confirmed that the main observations are robust and independent of the estimator (Figures S5–S7 in Supporting Information S1).

All the b^+ (and b-values) computed for the three eruptive stages are anomalously high compared to b-values found in tectonically driven environments; however, this is very common for volcanic regions (McNutt, 1996; Roberts et al., 2015; Wyss et al., 1997, 2001).

3.5. Observation 5: The Enhanced Eruption Catalog Reveals Structural Features of the Volcano

The relocated enhanced seismic catalog during the eruption has a comparable number of events to the catalog from 2001 to 2018. Thus, the new catalog illuminates the structures that were activated during the 2008 eruption at Okmok Volcano with an improved resolution. Figure 8 shows a map view and a cross section across the caldera with all events, VTs and LPs, color coded by time relative to the onset of the eruption.

The start of the eruption (red colors in Figure 8) is marked by earthquakes highly clustered under the active vents forming an elongated dipping structure as discussed in the opening sequence above (Section 3.2). During the eruption, the VT earthquakes close to Cone A are the only visible link between the deep (~5 km) earthquakes and the shallow seismicity (observed in Figure 2c and marked with a black dashed ellipse in 8b). We note in passing an intriguing feature that is present in both relocated catalogs. There is an inverted boot-shaped volume that has low earthquake density (red outline in Figure 8; see also Figures S1 and S2 in Supporting Information S1) that surrounds the 2008 eruption vents and roughly coincides with the deformation foci inferred by GPS and InSAR analysis (Lu & Dzurisin, 2010; Xue et al., 2020). The quiescence suggests a region unable to accommodate elastic stresses large enough to trigger detectable earthquakes perhaps due to either the heat of the shallow magma system weakening the rocks or unconsolidated caldera fill. This earthquake-poor region is robust to location procedures as shown in Figures S1–S4 in Supporting Information S1. Alternatively, the lack of shallow seismicity could also be explained by low stress levels near the surface only allowing the rupture of very small earthquakes which are challenging to detect even with advanced detection methods (e.g., Duputel et al., 2019) or by trains of VT earthquakes being recorded as tremor and not detected as individual earthquakes (Eibl et al., 2017).

4. Summary of Observations

The clustering and migrations described above is reinforced and summarized by the more formal analysis of Figure 9. We followed the procedure of Sect. 2.2 to compute a correlation matrix for VT and LP events, where we can identify clusters of earthquakes in time. For each of the main clusters, we also calculated an epicentral centroid by using the median latitude and median longitude. The high noise level of the site results in a modal cross-correlation value of ~0.4. Figure 9 emphasizes clusters that are much more correlated than this usual state
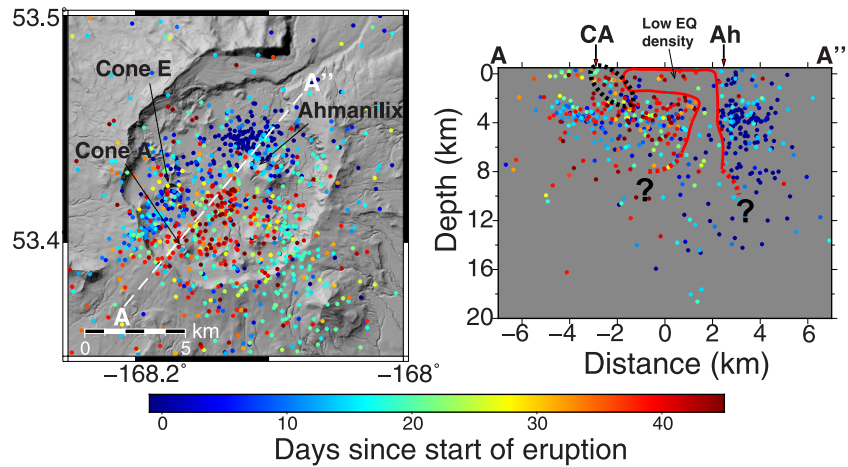
Figure 8. Relocated earthquake hypocenters using hypoDD for both VTs and LPs (colored by time since the eruption). The red-solid line indicates the volume of low earthquake density, coinciding with the initial source of deformation location from Lu and Dzurisin (2010), which progressed to depth over the course of the eruption. The dashed black ellipse indicates the only visible link of earthquakes that connect the 3–5 km deep cluster with Cone A. A vertical compression factor of 2× was applied to the cross-section. Width of cross-section = 2 km; azimuth = 40°. Arrows: CA = Cone A; Ah = Ahmanilix.

by using a color scale that is saturated at three standard deviations from the mean values. Please refer to the supporting information (Figure S10 in Supporting Information S1) to see the cross-correlation matrix without a saturated scale.

The short-term runup of seismicity leading to the eruption (July 12) shows a cluster of well-correlated VT earthquakes from 14:00-18:00 UTC and a secondary group of earthquakes between 18:00 and 19:00 UTC. The centroid location of these two clusters suggests that the focus of pre-eruptive activity shifted from directly beneath the North Vent and Ahmanilix to the southwest toward the deflation source within minutes to the onset of the eruption. These observations confirm the pre-eruptive chronology described in the opening sequence (Section 3.2) and it also matches the description by Ohlendorf et al. (2014), which noted the existence of these earthquake families. Thus, the correlation matrix quantitatively supports the visual identification of patterns discussed above.

Although the 48-hr rate of the LPs during the eruption shows they are related to venting processes (Figure 4b), the shorter-period 4-hr rate and the magnitude time series show that the timing of the LPs bursts is not coincident with the timing of the plumes. The highest degree of clustering observed for the co-eruptive stage corresponds to bursts of LPs (outline boxes in Figure 9 right hand panel), and their centroids track the migration pattern described in Section 3.1 (from Ahmanilix to the southeast caldera wall and Mount Tulik). The co-eruptive VT
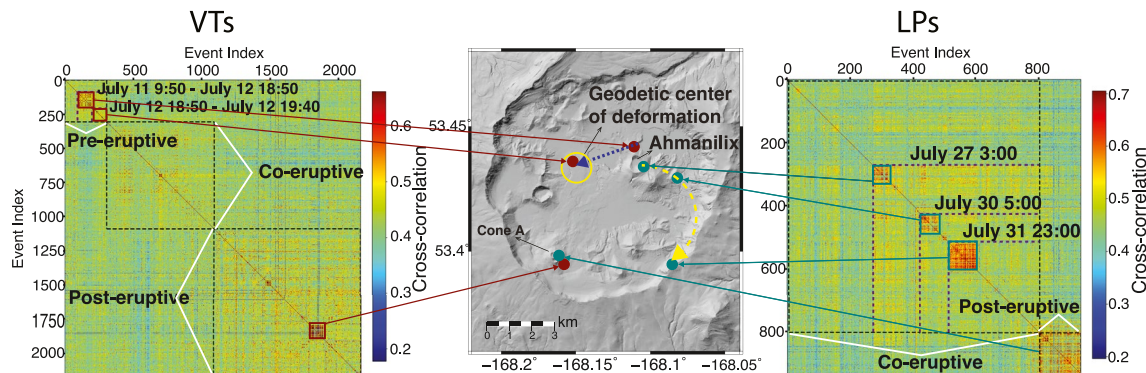

Figure 9. Cross-correlation matrix showing clustering. Events are sorted chronologically so low event indices correspond to the starting sequence and high indices correspond to post-eruptive earthquakes. The arrows point at the centroid of each cluster for the hypoDD relocations. Turquoise squares/arrows show LP activity. Red squares/arrows show VT activity. The dashed orange arrow shows the suggested precursory VT migration path toward the deflation source (yellow circle). The dashed yellow arrow shows the suggested co-eruptive LP migration path. The events are sorted in time following the numerical order. The locations of the co-eruptive VTs are not shown because they are broadly distributed.

earthquakes show a more stable rate than the LPs and they do not track the deflation rate observed in GPS (Figure 4a). The VTs have a lower degree of clustering for the co-eruptive earthquakes and the few well correlated VT events during this stage are clustered in the vicinity of Cone A.

The post-eruptive earthquakes occurred immediately after the last plumes observations, and they consist of a large burst of LP events that decayed rapidly in time (Figure 4b) and another large burst of VT events that decayed slowly in time (Figure 4a). These earthquakes in these post-eruptive bursts had lower magnitudes than those during the eruption. The clustering of these earthquakes is also visible in Figures 8 and 9. The centroids of the clusters are located near Cone A, and they occur mostly between 2 and 4 km depths (Figure 8). Note that these clusters correspond to significant events in the eruption chronology, however, most events are not in the outlined clusters in Figure 9. The differences in cluster centroids from the hypoDD and GrowClust relocations show slight variations but are not significant for our interpretation (Figure S11 in Supporting Information S1).

5. Discussion

The combined seismological observations of rates, spatio-temporal patterns, frequency classification, *b*-values, and clustering allow us to make a conceptual model of the 2008 eruption of Okmok Volcano (Figure 10) and interpret the mechanisms for the three main stages of the eruption: before, during and after.

The most striking and important observation here is the distinct behavior of the LP and VT events. Therefore, we will focus our analysis on the mechanisms that generate the LP and VT earthquakes and how these are related to eruption dynamics. As we will discuss, the LPs appear to be an indication of fluid flow and can track dynamic changes in clogging and cracking during the eruption, whereas the VTs respond to the deviatoric stresses in the host rocks as injection and extraction occur during the three main stages of the eruption (before, during and after). This is in good agreement with the perception that long period earthquakes are related to fluid flow and high frequency VTs are generated due to failure on faults (Benson et al., 2008; Foulger et al., 2004; Roman, 2005).

5.1. LPs Mechanism: Clog and Crack

LP earthquakes in volcanic systems have been attributed to effects such as resonance in fluid-filled cracks (Chouet, 1996; Haney et al., 2021; Kumagai & Chouet, 1999), brittle failure in melt (Goto, 1999; Neuberg et al., 2006), slow rupture in either heated material (Harrington & Brodsky, 2007) or in unconsolidated material (Bean et al., 2014) and magma degassing (Melnik et al., 2020). Migration and burstiness of long period earthquakes in volcanic systems have been previously reported for the preparatory stage of volcanic eruptions and associated with pore-pressure transients in a hydraulically connected plumbing system (Frank et al., 2018; Shapiro et al., 2017). For the 2008 eruption, no LPs (shallow or deep) preceded the eruption, they are only observed for the co- and post-eruptive stages, and to our knowledge this is the first report of migrating bursts of LPs that are not correlated in time with plumes during a long-lived explosive eruption.

The LP seismicity that is observed underneath the active vents during the middle of the eruption are undoubtedly related to the eruptive process and the immense amount of water accumulated in the subsurface of this area (Unema et al., 2016). The middle eruption sequence commenced with the drainage of North Lake, which probably interacted with the ascending magma causing increased fragmentation and elevating the explosivity (Gonnermann, 2015). Given the timing, location and migration of these low-frequency earthquakes, but more importantly their lack of association with plumes, our preferred model is a clog-and-crack mechanism: The open vents become partially clogged, potentially by their own collapse, which might be seen at the surface as widening, or by plugs of tephra, and other eruptive products, allowing for pressure to build up in the subsurface (Figure 10b). The clogging restricts the flow of incoming magma and volatiles to the atmosphere and increases the pore-pressure at the conduit, which forces the fluids into existing permeable cracks causing volumetric changes that translate into the solid medium as low-frequency seismic radiation (Chouet, 1988, 1996). An increase in pressure could also stress the surrounding heated or unconsolidated material to produce slow ruptures by brittle failure (Harrington & Brodsky, 2007). In either case, at some point, the accumulating pressure in the partially clogged system overcomes the clogging stress and cracks/opens triggering explosions that are followed by high altitude, dark (ash-rich) plumes and an LP rate reduction (Figure 10c). The energetic release of mass lasts until most of that pressure has been exhausted, allowing the re-clogging and triggering of a new LP burst. Note that there are few LPs still observed during the time of the emissions, which could be related to volumetric changes as the extraction of fluids takes place (Benson et al., 2008).
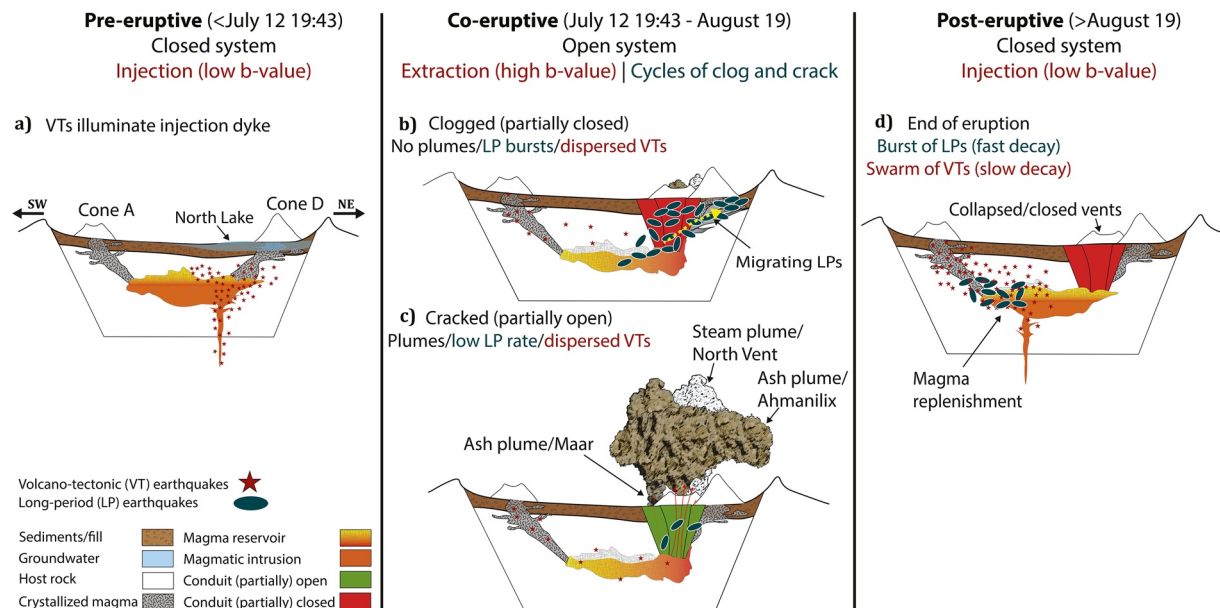
Figure 10. Cartoon of the evolution of the 2008 Okmok Volcano eruption. Left panel: (a) Activation of a swarm of volcano-tectonic earthquakes induced by the injection of magma from a deep source into a ~4 km depth shallow reservoir. The orientation of the cross-sectional view is SW-NE as indicated in panel (a) and it is the same for all other panels. At this stage the volcano is a closed system and there is a high rate of stress change as shown by a low *b*-value of the VTs. The SW of the caldera at Okmok Volcano has a higher content of groundwater and surface lakes, which explains the phreato-magmatic nature of the eruption. North Lake is shown in panel (a) due to its important role in the eruption. Center panel: After the eruption started following a large phreato-magmatic explosion, ash and steam plumes came out from at least four new major vents. During the extraction process the volcano is an open system and the stress and stressing rate are both lower than the initial phase (higher *b*-value of VTs). Toward the middle, North Lake drained into a vent and the eruption developed in cycles of clogging and cracking, potentially due to the collapse of the vents or changes in fragmentation. When the volcanic vents are clogged (b), long-period earthquake bursts migrate from the vents in the direction of the caldera wall. When the volcano overcomes the clogging stress and the vents are cracked open (c), there is mass transfer of fluids and ash into the atmosphere and very few earthquakes are observed. Right panel: (d) the end of the eruption is marked by a burst of long-period earthquakes that is accompanied and followed by a cascade of VT earthquakes, distributed in the south of the caldera. At this stage there was injection of magma into the shallow magma reservoir that increased the stress regime but that resulted in a failed intrusion. After this the volcano remained closed.

The clog-and-crack scenario presented above resembles the valve opening/closing mechanism by Farge et al. (2021). This mechanism was proposed to explain low-frequency seismicity in subduction zones as bursts of tremor migrate along channels that experience abrupt changes in permeability when they get clogged by particles (closed valve) and unclogged by flow-induced stresses (open valve). The model by Farge et al. (2021) shows the emergence of the bursty and migratory behavior of low-frequency earthquakes, which is exactly what we observe for the co-eruptive LPs at Okmok Volcano.

The climatic middle sequence culminated as LPs gave way to a migrating high amplitude tremor at the vents (Haney, 2014) and the last large, ash-rich plumes of the eruption. The volcano seemed to have lost most of its eruptive power during these cycles of LPs and plumes events, and the eruption began to abate until the last emission was observed on August 19.

The last burst of LP events, which occurred after the last plume emissions, likely indicates the filling of available cracks with magmatic fluids and gasses as the system remained permanently clogged and the shallow reservoir started to refill again (Figure 10d). This observation is supported by the relocation depth of the post-eruptive earthquakes' hypocenters (Figure 8), which coincides with the depths of the magma reservoir suggested by other authors.

The clog-and-crack model presented here differs from the more general discussions of the significance of open and closed vent systems. The term "open system" is often used for degassing behavior and is used to highlight how degassing behavior can be distinct from magma discharge behavior (e.g., Edmonds et al., 2022). Here, we only constrain the existence or not of plumes and have no direct constraints on the degassing and its relationship to magmatic processes. Furthermore, open volcanic systems in the degassing sense have been associated with high LP rates (Roman et al., 2019), whereas our "unclogged" system has a low LP rate during magmatic discharge.

In principle, another possibility is that one mechanism creates the LPs directly underneath the vents and a different one creates those close to the caldera wall and other intra-caldera cones (A and C). The LPs underneath the vent could be signaling strain-induced changes in fragmentation as magma batches migrate toward the surface (Gonnermann, 2015; Papale, 1999), whereas the LPs close to the caldera wall could be the manifestation of slow slip in patches of the ring fault structure. Such complexity cannot be ruled out, but the binary classification scheme used here does not find any distinction between the waveforms of the caldera wall and intra-caldera populations and the more complicated explanation is not favored for the migrating bursts simply because of the relationship to the plume emissions.

5.2. VTs Mechanism: Brittle Failure as Stress Gauges

Whether they are triggered by magmatic intrusions or not, VT earthquakes are the signature of brittle failure in the rocks that make a volcano and its surroundings. Physically, they are not different from earthquakes that occur in non-volcanic media, and even their ability to trigger aftershocks is the same as non-volcanic earthquakes (Garza-Girón et al., 2018). Thus, they must also obey elastic and friction laws that depend on stressing rate changes in the medium (Dieterich, 1994; Kanamori & Brodsky, 2004). It is well known that the stress increase induced by the emplacement of dykes can cause large changes in seismicity rate of VT earthquakes, which are commonly matched by observations of crustal deformation (Dieterich et al., 2000; Rivalta et al., 2015; Segall, 2013). Consequently, analysis of VT earthquakes has become instrumental in forecasting eruptions (Roman et al., 2006; Ruppert et al., 2011; White & McCausland, 2016). However, little is known about the behavior of VTs during the extraction that takes place while the volcano is erupting. The observations presented here, based on seismicity rates, spatio-temporal patterns and changes in b-values, provide insight into the response of the rocks before, during and after the eruption as the volcanic system experienced injection, extraction and re-injection.

The largest changes in seismicity rate for the VTs are before and after the eruption (Figure 4). The runup seismicity is an example of earthquakes induced by stress changes likely caused by the injection of the dyke that triggered the eruption, and VTs are thought to display different spatio-temporal patterns depending on the triggering mechanism related to the magma migration, which can vary from one eruption to another (Roman & Cashman, 2006). The pre-eruptive earthquakes observed here do not show a clear upward trend (i.e., vertical migration). Instead, they were distributed around the dyke, although they may have concentrated at ∼4 km of depth about an hour before the eruption (Figures 6b and 6c). Therefore, we infer that, for this eruption, VTs were not predominantly triggered at the tip of the propagating dyke where one might expect the local elastic stress changes to be highest. Rather, the stress changes, promoted by the intrusion, induced slip on pre-stressed faults, as has been previously inferred for other dike intrusions (Roman, 2005; Rubin & Gillard, 1998).

The clog-and-crack systematics are manifested in the LP rate. However, the VTs that we measured do offer additional insight into the opening and closing of the system over a longer timescale. If high b-values indicate low stresses as suggested in prior work (Scholz, 1968, 2015), then the time variation of b^+ values of VT events (Figure 7) indicates that the elastic stresses in the edifice and surrounding rock were lower during the eruption than before and after. Evidently, the pre-eruptive sequence was triggered by an intrusion, so the VT generation is an indication of the stress accumulated in the subsurface as a closed system (low b^+) became highly pressurized due to the injection of magma (Figure 10a). Following the first blasts, the volcano became an open system, and the rocks experienced a reduction in deviatoric stresses (high b^+) as the eruption extracted material (middle panel in Figure 10). An increase in b-values after the onset of the eruption has also been observed in other eruptions (Shakirova & Firstov, 2022), but other eruptions have shown an opposite pattern with lower b-values after the onset of the eruption (Ibáñez et al., 2012). During the co-eruptive stage, VTs showed a steadier rate than the LPs and they did not follow the GPS deflation rate, implying that reservoir deflation was not the main source of stress during the eruption. Finally, for the post-eruptive phase (Figure 10d), the steadily decaying cascade of VT earthquakes immediately after the last emission, which were initially accompanied by a prominent burst of LPs that decayed quickly, are indicative of a large change in the stressing regime and faults being able to accumulate and release elastic strain again. Since the GPS station OKCE located inside the caldera (Cone E) showed a re-inflation signal when it was fixed by AVO staff shortly after the eruption ended, we interpret this as the seismic signature of a closed system (low b^+) which was stressed by an immediate reservoir replenishment process (i.e., an intrusion drawn into low-pressure pockets without overcoming the final clogging stress).

6. Conclusions

We analyzed an enhanced, relocated and frequency-classified (VT and LP) earthquake catalog during an explosive volcanic eruption. The analysis shows that with such advanced data processing, we can illuminate the structure of the volcano with high resolution and gain information on fundamental dynamic interactions between the solid and fluid media during the eruption. The co-eruptive LP and VT events demonstrate distinct behavior, likely caused by and therefore diagnostic of different eruptive processes. LPs are strongly localized in space and time and directly precede or follow mass ejection, contrasting with the steady, widely distributed VTs.

Together, the seismicity defined how the eruption began, evolved, and ended, which is a major goal for volcanology (National Academies of Sciences, 2017). The 2008 explosive eruption started with the injection of magma from a deep reservoir which triggered a swarm of VTs that were randomly distributed about the dyke. Minutes before the eruption, VTs migrated toward the geodetic center of deformation shown by other authors. The eruption then evolved through at least three opening and closing cycles that showed a distinctive pattern of seismicity that we term clog-and-crack. A high seismicity rate half-way through the eruption discloses a series of migratory LP earthquakes that started with a burst directly beneath the eruptive vent, followed by ash-rich plumes, and continued to the east and southeast with two other main bursts that were also followed by dark (ash-rich) plumes. The eruption also involved a distinct population of VT earthquakes that maintain a steadier rate over a large region of the caldera. These co-eruptive VTs have a higher b-value than before or after the eruption, suggesting that the extraction process induced lower levels of stress in the caldera than the pre- and post-eruptive injection. The end of the eruptive activity is marked by a sudden burst of LP earthquakes which are accompanied and followed by a steady stream of small VT earthquakes that occur south (and therefore distinct) from the previous concentration of seismicity. Given the association of LP events with the previous pressurization episodes, it is possible that the end of the eruption was marked by another intrusion that failed to reach the surface and thus sealed the system.

An overriding theme is the repeated closure with clogged vents, as signaled by the localized LPs and subsequent opening with eruptive plumes. Even the closure of the eruption appears to have been a variation of this cycle. The high-speed evolution of the vent and pressurization of the rock can be illuminated through these previously inaccessible observations and has provided new clarity into the stages of the 2008 Okmok Volcano eruption. In the future, advanced seismic processing pipelines may allow for a similar analysis which could help volcano observatories gain more insight into the eruptive dynamics in near real-time and allow decision makers during volcanic crises to benefit from seeing the eruptions clearly.

Data Availability Statement

The catalogs used in this work are available at https://zenodo.org/record/7682936.

References

Aki, K. (1965). Maximum likelihood estimate of b in the formula log N= a-bM and its confidence limits. *Bulletin of Earthquake Research Institute, Tokyo University*, *43*, 237–239.

Albright, J. A., Gregg, P. M., Lu, Z., & Freymueller, J. T. (2019). Hindcasting magma reservoir stability preceding the 2008 eruption of Okmok, Alaska. *Geophysical Research Letters*, *46*(15), 8801–8808. https://doi.org/10.1029/2019gl083395

Bean, C. J., De Barros, L., Lokmer, I., Métaxian, J. P., O'Brien, G., & Murphy, S. (2014). Long-period seismicity in the shallow volcanic edifice formed from slow-rupture earthquakes. *Nature Geoscience*, *7*(1), 71–75. https://doi.org/10.1038/ngeo2027

Benoit, J. P., & McNutt, S. R. (1996). Global volcanic earthquake swarm database and preliminary analysis of volcanic earthquake swarm duration. *Annali di Geofisica*, *39*(2), 221.

Benson, P. M., Vinciguerra, S., Meredith, P. G., & Young, R. P. (2008). Laboratory simulation of volcano seismicity. *Science*, *322*(5899), 249–252. https://doi.org/10.1126/science.1161927

Beyreuther, M., Barsch, R., Krischer, L., Megies, T., Behr, Y., & Wassermann, J. (2010). ObsPy: A Python toolbox for seismology. *Seismological Research Letters*, *81*(3), 530–533. https://doi.org/10.1785/gssrl.81.3.530

Biggs, J., Lu, Z., Fournier, T., & Freymueller, J. T. (2010). Magma flux at Okmok Volcano, Alaska, from a joint inversion of continuous GPS, campaign GPS, and interferometric synthetic aperture radar. *Journal of Geophysical Research*, *115*(B12), B12401. https://doi.org/10.1029/2010jb007577

Bridges, D. L., & Gao, S. S. (2006). Spatial variation of seismic 1alues beneath Makushin volcano, Unalaska island, Alaska. *Earth and Planetary Science Letters*, *245*(1–2), 408–415. https://doi.org/10.1016/j.epsl.2006.03.010

Buurman, H., West, M. E., & Power, J. A. (2006). Seismic precursors to volcanic explosions during the 2006 eruption of Augustine Volcano. *Professional Paper 1769-2*, 41–57.

Caudron, C., Taisne, B., Kugaenko, Y., & Saltykov, V. (2015). Magma migration at the onset of the 2012–13 Tolbachik eruption revealed by seismic amplitude ratio analysis. *Journal of Volcanology and Geothermal Research*, *307*, 60–67. https://doi.org/10.1016/j.jvolgeores.2015.09.010

Chouet, B. (1988). Resonance of a fluid-driven crack: Radiation properties and implications for the source of long-period events and harmonic tremor. *Journal of Geophysical Research*, *93*(B5), 4375–4400. https://doi.org/10.1029/jb093ib05p04375

Chouet, B. A. (1996). Long-period volcano seismicity: Its source and use in eruption forecasting. *Nature*, *380*(6572), 309–316. https://doi.org/10.1038/380309a0

Coats, R. R. (1950). *Volcanic activity in the Aleutian arc* (pp. 35–49). US Government Printing Office.

D'Auria, L., Koulakov, I., Prudencio, J., Cabrera-Pérez, I., Ibáñez, J. M., Barrancos, J., et al. (2022). Rapid magma ascent beneath La Palma revealed by seismic tomography. *Scientific Reports*, *12*(1), 17654. https://doi.org/10.1038/s41598-022-21818-9

Dieterich, J. (1994). A constitutive law for rate of earthquake production and its application to earthquake clustering. *Journal of Geophysical Research*, *99*(B2), 2601–2618. https://doi.org/10.1029/93jb02581

Dieterich, J., Cayol, V., & Okubo, P. (2000). The use of earthquake rate changes as a stress meter at Kilauea volcano. *Nature*, *408*(6811), 457–460. https://doi.org/10.1038/35044054

Duputel, Z., Lengliné, O., & Ferrazzini, V. (2019). Constraining spatiotemporal characteristics of magma migration at Piton de la Fournaise volcano from pre-eruptive seismicity. *Geophysical Research Letters*, *46*(1), 119–127. https://doi.org/10.1029/2018gl080895

Edmonds, M., Liu, E. J., & Cashman, K. V. (2022). Open-vent volcanoes fuelled by depth-integrated magma degassing. *Bulletin of Volcanology*, *84*(3), 1–27. https://doi.org/10.1007/s00445-021-01522-8

Eibl, E. P., Bean, C. J., Vogfjörd, K. S., Ying, Y., Lokmer, I., Möllhoff, M., et al. (2017). Tremor-rich shallow dyke formation followed by silent magma flow at Bárðarbunga in Iceland. *Nature Geoscience*, *10*(4), 299–304. https://doi.org/10.1038/ngeo2906

Farge, G., Jaupart, C., & Shapiro, N. M. (2021). Episodicity and migration of low frequency earthquakes modeled with fast fluid pressure transients in the permeable subduction interface. *Journal of Geophysical Research: Solid Earth*, *126*(9), e2021JB021894. https://doi.org/10.1029/2021jb021894

Foulger, G. R., Julian, B. R., Hill, D. P., Pitt, A. M., Malin, P. E., & Shalev, E. (2004). Non-double-couple microearthquakes at long valley caldera, California, provide evidence for hydraulic fracturing. *Journal of Volcanology and Geothermal Research*, *132*(1), 45–71. https://doi.org/10.1016/s0377-0273(03)00420-7

Fournier, T., Freymueller, J., & Cervelli, P. (2009). Tracking magma volume recovery at Okmok volcano using GPS and an unscented Kalman filter. *Journal of Geophysical Research*, *114*(B2), B02405. https://doi.org/10.1029/2008JB005837

Frank, W. B., Shapiro, N. M., & Gusev, A. A. (2018). Progressive reactivation of the volcanic plumbing system beneath Tolbachik volcano (Kamchatka, Russia) revealed by long-period seismicity. *Earth and Planetary Science Letters*, *493*, 47–56. https://doi.org/10.1016/j.epsl.2018.04.018

Freymueller, J. T., & Kaufman, A. M. (2010). Changes in the magma system during the 2008 eruption of Okmok volcano, Alaska, based on GPS measurements. *Journal of Geophysical Research*, *115*(B12), B12415. https://doi.org/10.1029/2010jb007716

Garza-Girón, R. (2014). Spatial variation of the b value under Popocatepetl Volcano and its relation with the magma chamber. (428928) [Bachelor's dissertation, Universidad Nacional Autónoma de México, México]. Repositorio de Tesis DGBSDI. Retrieved from https://repositorio.unam.mx/contenidos/428928

Garza-Girón, R., Brodsky, E. E., & Prejean, S. G. (2018). Mainshock-aftershock clustering in volcanic regions. *Geophysical Research Letters*, *45*(3), 1370–1378. https://doi.org/10.1002/2017gl075738

Garza-Girón, R., Brodsky, E. E., Spica, Z. J., Haney, M. M., & Webley, P. W. (2023). A specific earthquake processing workflow for studying long-lived, explosive volcanic eruptions with application to the 2008 Okmok Volcano, Alaska, eruption. *Journal of Geophysical Research: Solid Earth*, *128*(5), e2022JB025882. https://doi.org/10.1029/2022jb025882

Gerstenberger, M., Wiemer, S., & Giardini, D. (2001). A systematic test of the hypothesis that the b value varies with depth in California. *Geophysical Research Letters*, *28*(1), 57–60. https://doi.org/10.1029/2000gl012026

Gonnermann, H. M. (2015). Magma fragmentation. *Annual Review of Earth and Planetary Sciences*, *43*(1), 431–458. https://doi.org/10.1146/annurev-earth-060614-105206

Goto, A. (1999). A new model for volcanic earthquake at Unzen Volcano: Melt rupture model. *Geophysical Research Letters*, *26*(16), 2541–2544. https://doi.org/10.1029/1999gl900569

Grey, D. M. (2003). Post-caldera eruptions at Okmok volcano, Umnak Island, Alaska, with emphasis on recent eruptions from Cone A (Doctoral dissertation).

Haney, M. M. (2010). Location and mechanism of very long period tremor during the 2008 eruption of Okmok Volcano from interstation arrival times. *Journal of Geophysical Research*, *115*(B10), B00B05. https://doi.org/10.1029/2010jb007440

Haney, M. M. (2014). Backprojection of volcanic tremor. *Geophysical Research Letters*, *41*(6), 1923–1928. https://doi.org/10.1002/2013gl058836

Haney, M. M., Buurman, H., Holtkamp, S., & McNutt, S. R. (2021). Monochromatic long-period seismicity prior to the 2012 earthquake swarm at little Sitkin volcano, Alaska. *Frontiers in Earth Science*, *9*, 513. https://doi.org/10.3389/feart.2021.689651

Harrington, R. M., & Brodsky, E. E. (2007). Volcanic hybrid earthquakes that are brittle-failure events. *Geophysical Research Letters*, *34*(6), L06308. https://doi.org/10.1029/2006gl028714

Ibáñez, J. M., De Angelis, S., Díaz-Moreno, A., Hernández, P., Alguacil, G., Posadas, A., & Pérez, N. (2012). Insights into the 2011–2012 submarine eruption off the coast of El Hierro (Canary Islands, Spain) from statistical analyses of earthquake activity. *Geophysical Journal International*, *191*(2), 659–670. https://doi.org/10.1111/j.1365-246x.2012.05629.x

Johnson, J. H., Prejean, S., Savage, M. K., & Townend, J. (2010). Anisotropy, repeating earthquakes, and seismicity associated with the 2008 eruption of Okmok volcano, Alaska. *Journal of Geophysical Research*, *115*(B9), B00B04. https://doi.org/10.1029/2009jb006991

Kanamori, H., & Brodsky, E. E. (2004). The physics of earthquakes. *Reports on Progress in Physics*, *67*(8), 1429–1496. https://doi.org/10.1088/0034-4885/67/8/r03

Kumagai, H., & Chouet, B. A. (1999). The complex frequencies of long-period seismic events as probes of fluid composition beneath volcanoes. *Geophysical Journal International*, *138*(2), F7–F12. https://doi.org/10.1046/j.1365-246x.1999.00911.x

Larsen, J., Neal, C., Webley, P., Freymueller, J., Haney, M., McNutt, S., et al. (2009). Eruption of Alaska volcano breaks historic pattern. *Eos, Transactions American Geophysical Union*, *90*(20), 173–174. https://doi.org/10.1029/2009eo200001

Larsen, J., Neal, C. A., Schaefer, J. R., Kaufman, M., & Lu, Z. (2015). *The 2008 phreatomagmatic eruption of Okmok Volcano, Aleutian islands, Alaska: Chronology, deposits, and landform changes (No. RI 2015-2)*. Alaska Division of Geological and Geophysical Surveys.

Lengliné, O., Duputel, Z., & Okubo, P. G. (2021). Tracking dike propagation leading to the 2018 Kīlauea eruption. *Earth and Planetary Science Letters*, *553*, 116653. https://doi.org/10.1016/j.epsl.2020.116653

Lu, Z., & Dzurisin, D. (2010). Ground surface deformation patterns, magma supply, and magma storage at Okmok Volcano, Alaska, from InSAR analysis: 2. Coeruptive deflation, July–August 2008. *Journal of Geophysical Research*, *115*(B5), B00B03. https://doi.org/10.1029/2009jb006970

Lu, Z., Masterlark, T., & Dzurisin, D. (2005). Interferometric synthetic aperture study of Okmok volcano, Alaska: Magma supply dynamics and post-emplacement lava flow deformation. *Journal of Geophysical Research*, *110*(B2), B02403. https://doi.org/10.1029/2004JB003148

Mann, D., Freymueller, J., & Lu, Z. (2002). Deformation associated with the 1997 eruption of Okmok volcano, Alaska. *Journal of Geophysical Research*, *107*(B4), 1–7. ETG 7-1–ETG 7-12. https://doi.org/10.1029/2001JB000163

Masterlark, T., Haney, M., Dickinson, H., Fournier, T., & Searcy, C. (2010). Rheologic and structural controls on the deformation of Okmok Volcano, Alaska: FEMs, InSAR, and ambient noise tomography. *Journal of Geophysical Research*, *115*(B2), B02409. https://doi.org/10.1029/2009jb006324

McNutt, S. R. (1996). Seismic monitoring and eruption forecasting of volcanoes: A review of the state-of-the-art and case histories. *Monitoring and mitigation of volcano hazards*, 99–146. https://doi.org/10.1007/978-3-642-80087-0_3

Melnik, O., Lyakhovsky, V., Shapiro, N. M., Galina, N., & Bergal-Kuvikas, O. (2020). Deep long period volcanic earthquakes generated by degassing of volatile-rich basaltic magmas. *Nature Communications*, *11*(1), 3918. https://doi.org/10.1038/s41467-020-17759-4

Mogi, K. (1963). Some discussions on aftershocks, foreshocks and earthquake swarms: The fracture of a semi-infinite body caused by an inner stress origin and its relation to the earthquake phenomena (third paper). 東京大學地震研究所彙報= *Bulletin of the Earthquake Research Institute, University of Tokyo*, *41*(3), 615–658.

National Academies of Sciences, Engineering and Medicine. (2017). *Volcanic eruptions and their repose, unrest, precursors, and timing*. National Academies Press.

Neuberg, J. W., Tuffen, H., Collier, L., Green, D., Powell, T., & Dingwell, D. (2006). The trigger mechanism of low-frequency earthquakes on Montserrat. *Journal of Volcanology and Geothermal Research*, *153*(1–2), 37–50. https://doi.org/10.1016/j.jvolgeores.2005.08.008

Newhall, C. G., & Self, S. (1982). The volcanic explosivity index (VEI) an estimate of explosive magnitude for historical volcanism. *Journal of Geophysical Research*, *87*(C2), 1231–1238. https://doi.org/10.1029/jc087ic02p01231

Ohlendorf, S. J., Thurber, C. H., Pesicek, J. D., & Prejean, S. G. (2014). Seismicity and seismic structure at Okmok Volcano, Alaska. *Journal of Volcanology and Geothermal Research*, *278*, 103–119. https://doi.org/10.1016/j.jvolgeores.2014.04.002

Papale, P. (1999). Strain-induced magma fragmentation in explosive eruptions. *Nature*, *397*(6718), 425–428. https://doi.org/10.1038/17109

Petersen, T. (2007). Swarms of repeating long-period earthquakes at Shishaldin Volcano, Alaska, 2001–2004. *Journal of Volcanology and Geothermal Research*, *166*(3–4), 177–192. https://doi.org/10.1016/j.jvolgeores.2007.07.014

Power, J. A., Friberg, P. A., Haney, M. M., Parker, T., Stihler, S. D., & Dixon, J. P. (2019). *A unified catalog of earthquake hypocenters and magnitudes at volcanoes in Alaska—1989 to 2018* (No. 2019-5037). US Geological Survey.

Rivalta, E., Taisne, B., Bunger, A. P., & Katz, R. F. (2015). A review of mechanical models of dike propagation: Schools of thought, results and future directions. *Tectonophysics*, *638*, 1–42. https://doi.org/10.1016/j.tecto.2014.10.003

Roberts, N. S., Bell, A. F., & Main, I. G. (2015). Are volcanic seismic b-values high, and if so when? *Journal of Volcanology and Geothermal Research*, *308*, 127–141. https://doi.org/10.1016/j.jvolgeores.2015.10.021

Roman, D. C. (2005). Numerical models of volcanotectonic earthquake triggering on non-ideally oriented faults. *Geophysical Research Letters*, *32*(2), L02304. https://doi.org/10.1029/2004gl021549

Roman, D. C., & Cashman, K. V. (2006). The origin of volcano-tectonic earthquake swarms. *Geology*, *34*(6), 457–460. https://doi.org/10.1130/g22269.1

Roman, D. C., LaFemina, P. C., Bussard, R., Stephens, K., Wauthier, C., Higgins, M., et al. (2019). Mechanisms of unrest and eruption at persistently restless volcanoes: Insights from the 2015 eruption of Telica Volcano, Nicaragua. *Geochemistry, Geophysics, Geosystems*, *20*(8), 4162–4183. https://doi.org/10.1029/2019gc008450

Roman, D. C., Neuberg, J., & Luckett, R. R. (2006). Assessing the likelihood of volcanic eruption through analysis of volcanotectonic earthquake fault–plane solutions. *Earth and Planetary Science Letters*, *248*(1–2), 244–252. https://doi.org/10.1016/j.epsl.2006.05.029

Rubin, A. M., & Gillard, D. (1998). Dike-induced earthquakes: Theoretical considerations. *Journal of Geophysical Research*, *103*(B5), 10017–10030. https://doi.org/10.1029/97jb03514

Ruppert, N. A., Prejean, S., & Hansen, R. A. (2011). Seismic swarm associated with the 2008 eruption of Kasatochi Volcano, Alaska: Earthquake locations and source parameters. *Journal of Geophysical Research*, *116*(B2), B00B07. https://doi.org/10.1029/2010jb007435

Scholz, C. H. (1968). The frequency-magnitude relation of microfracturing in rock and its relation to earthquakes. *Bulletin of the Seismological Society of America*, *58*(1), 399–415. https://doi.org/10.1785/bssa0580010399

Scholz, C. H. (2015). On the stress dependence of the earthquake b value. *Geophysical Research Letters*, *42*(5), 1399–1402. https://doi.org/10.1002/2014gl062863

Schorlemmer, D., Wiemer, S., & Wyss, M. (2005). Variations in earthquake-size distribution across different stress regimes. *Nature*, *437*(7058), 539–542. https://doi.org/10.1038/nature04094

Segall, P. (2013). Volcano deformation and eruption forecasting. *Geological Society, London, Special Publications*, *380*(1), 85–106. https://doi.org/10.1144/sp380.4

Seropian, G., Kennedy, B. M., Walter, T. R., Ichihara, M., & Jolly, A. D. (2021). A review framework of how earthquakes trigger volcanic eruptions. *Nature Communications*, *12*(1), 1–13. https://doi.org/10.1038/s41467-021-21166-8

Shakirova, A., & Firstov, P. (2022). Features of the Kizimen Volcano area seismicity prior to and during the 2010–2013 eruption. *Journal of Volcanology and Geothermal Research*, *421*, 107420. https://doi.org/10.1016/j.jvolgeores.2021.107420

Shapiro, N. M., Droznin, D. V., Droznina, S. Y., Senyukov, S. L., Gusev, A. A., & Gordeev, E. I. (2017). Deep and shallow long-period volcanic seismicity linked by fluid-pressure transfer. *Nature Geoscience*, *10*(6), 442–445. https://doi.org/10.1038/ngeo2952

Thelen, W., Malone, S., & West, M. (2011). Multiplets: Their behavior and utility at dacitic and andesitic volcanic centers. *Journal of Geophysical Research*, *116*(B8), B08210. https://doi.org/10.1029/2010jb007924

Trugman, D. T., & Shearer, P. M. (2017). GrowClust: A hierarchical clustering algorithm for relative earthquake relocation, with application to the Spanish Springs and Sheldon, Nevada, earthquake sequences. *Seismological Research Letters*, *88*(2A), 379–391. https://doi.org/10.1785/0220160188

Umakoshi, K., Takamura, N., Shinzato, N., Uchida, K., Matsuwo, N., & Shimizu, H. (2008). Seismicity associated with the 1991–1995 dome growth at Unzen Volcano, Japan. *Journal of Volcanology and Geothermal Research*, *175*(1–2), 91–99. https://doi.org/10.1016/j.jvolgeores.2008.03.030

Unema, J. A., Ort, M. H., Larsen, J. F., Neal, C. A., & Schaefer, J. R. (2016). Water-magma interaction and plume processes in the 2008 Okmok eruption, Alaska. *Bulletin*, *128*(5–6), 792–806. https://doi.org/10.1130/b31360.1

Utsu, T. (1965). A method for determining the value of" b" in a formula log n= a-bm showing the magnitude-frequency relation for earthquakes. *Geophysical Bulletin of Hokkaido University*, *13*, 99–103.

Van der Elst, N. J. (2021). B-positive: A robust estimator of aftershock magnitude distribution in transiently incomplete catalogs. *Journal of Geophysical Research: Solid Earth*, *126*(2), e2020JB021027. https://doi.org/10.1029/2020jb021027

Vergniolle, S., & Métrich, N. (2021). Open-vent volcanoes: A preface to the special issue. *Bulletin of Volcanology*, *83*(5), 29. https://doi.org/10.1007/s00445-021-01454-3

Waldhauser, F., & Ellsworth, W. L. (2000). A double-difference earthquake location algorithm: Method and application to the northern Hayward fault, California. *Bulletin of the Seismological Society of America*, *90*(6), 1353–1368. https://doi.org/10.1785/0120000006

Wang, J., Lu, Z., & Gregg, P. M. (2021). Inflation of Okmok volcano during 2008–2020 from PS analyses and source inversion with finite element models. *Journal of Geophysical Research: Solid Earth*, *126*(10), e2021JB022420. https://doi.org/10.1029/2021jb022420

Wessel, P., Luis, J. F., Uieda, L., Scharroo, R., Wobbe, F., Smith, W. H. F., & Tian, D. (2019). The generic mapping tools version 6. *Geochemistry, Geophysics, Geosystems*, *20*(11), 5556–5564. https://doi.org/10.1029/2019gc008515

White, R., & McCausland, W. (2016). Volcano-Tectonic earthquakes: A new tool for estimating intrusive volumes and forecasting eruptions. *Journal of Volcanology and Geothermal Research*, *309*, 139–155. https://doi.org/10.1016/j.jvolgeores.2015.10.020

Wiemer, S., & Wyss, M. (2000). Minimum magnitude of completeness in earthquake catalogs: Examples from Alaska, the Western United States, and Japan. *Bulletin of the Seismological Society of America*, *90*(4), 859–869. https://doi.org/10.1785/0119990114

Wyss, M., Klein, F., Nagamine, K., & Wiemer, S. (2001). Anomalously high b-values in the south Flank of Kilauea volcano, Hawaii: Evidence for the distribution of magma below Kilauea's east rift zone. *Journal of Volcanology and Geothermal Research*, *106*(1–2), 23–37. https://doi.org/10.1016/s0377-0273(00)00263-8

Wyss, M., Shimazaki, K., & Wiemer, S. (1997). Mapping active magma chambers by b values beneath the off-Ito volcano, Japan. *Journal of Geophysical Research*, *102*(B9), 20413–20422. https://doi.org/10.1029/97jb01074

Xue, X., Freymueller, J., & Lu, Z. (2020). Modeling the posteruptive deformation at Okmok based on the GPS and InSAR time series: Changes in the shallow magma storage system. *Journal of Geophysical Research: Solid Earth*, *125*(2), e2019JB017801. https://doi.org/10.1029/2019jb017801

Zobin, V. M. (2012). *Introduction to volcanic seismology* (2nd ed.). Elsevier.